Computational Modeling of Dual-Phase Ceramics with Finsler-Geometric Phase Field Mechanics

John D. Clayton[1, *]

Abstract: A theory invoking concepts from differential geometry of generalized Finsler space in conjunction with diffuse interface modeling is described and implemented in finite element (FE) simulations of dual-phase polycrystalline ceramic microstructures. Order parameters accounting for fracture and other structural transformations, notably partial dislocation slip, twinning, or phase changes, are dimensionless entries of an internal state vector of generalized pseudo-Finsler space. Ceramics investigated in computations are a boron carbide-titanium diboride (B_4C-TiB_2) composite and a diamond-silicon carbide (C-SiC) composite. Deformation mechanisms-in addition to elasticity and cleavage fracture in grains of any phase-include restricted dislocation glide (TiB_2 phase), deformation twinning (B_4C and β-SiC phases), and stress-induced amorphization (B_4C phase). The metric tensor of generalized Finsler space is scaled conformally according to dilatation induced by cavitation or other fracture modes and densification induced by phase changes. Simulations of pure shear consider various morphologies and lattice orientations. Effects of microstructure on overall strength of each composite are reported. In B_4C-TiB_2, minor improvements in shear strength and ductility are observed with an increase in the second phase from 10 to 18% by volume, suggesting that residual stresses or larger-scale crack inhibition may be responsible for toughness gains reported experimentally. In diamond-SiC, a composite consisting of diamond crystals encapsulated in a nano-crystalline SiC matrix shows improved strength and ductility relative to a two-phase composite with isolated bulk SiC grains.

Keywords: Micromechanics, ceramic composites, Finsler space, differential geometry, phase field, finite elements.

1 Introduction

Polycrystalline ceramics are solid materials that generally are mechanically stiff yet prone to brittle fracture. Heterogeneous composite ceramics consisting of grains of different chemical compositions or phases have been engineered to provide increased strength, ductility, and toughness relative to monolithic ceramics.

[1]US ARL, Impact Physics Branch, Aberdeen Proving Ground, MD, 21005-5066, USA.
*Corresponding Author: John D. Clayton. Email: john.d.clayton1.civ@mail.mil.

The current work focuses on two such ceramic composites, each consisting of two distinct phases. One such dual-phase material contains mostly crystalline boron carbide (B_4C, trigonal structure) interspersed with secondary grains of crystalline titanium diboride (TiB_2, hexagonal structure), wherein grain sizes of both phases are comparable. Versions of this material system are discussed in sigl et al. [Sigl and Kleebe (1995); White and Dickey (2011)]. Single-phase boron carbide is prone to brittle failure by cleavage, and at high stresses, may undergo a phase change to an amorphous solid as well as deform by deformation twinning [Chen, McCauley and Hemker (2003); Clayton (2012); An and Goddard (2015)]. Titanium diboride may impart higher fracture resistance by cleavage crack deflection or bridging, and some ductililty may be afforded by dislocation motion that has been suggested from shock experiments [Vanderwalker and Croft (1988)]. Compressive residual stresses induced in B_4C from TiB_2 by thermal processing may also improve performance.

The second dual-phase material studied is comprised of diamond crystals (C, cubic structure) either interspersed with or encapsulated by silicon carbide micro- or nano-crystals (β-SiC, cubic structure). Though the hardest of natural materials, diamond is prone to cleavage fracture, and incorporation of a softer SiC phase appears to improve overall toughness [Zhao, Qian, Daemen et al. (2004)]. As with the other composite, possible reasons include crack deflection at grain and phase boundaries as well as compressive residual stresses in grains of the stiffer phase. Twinning is also prevalent in β-SiC as a result of its low stacking fault energy [Van Torne (1966); Ning and Ye (1990)].

This paper invokes, in FE simulations, a theory combining aspects of phase field mechanics and differential geometry on generalized Finsler spaces. Perhaps the most comprehensive description of this model, including versions accounting for multiple inelastic deformation mechanisms, finite strain kinematics, and nonlinear elasticity, is given in Clayton et al. [Clayton and Knap (2018a)]. A pseudo-Finsler metric tensor is assigned that depends on a vector of internal state variables, whose entries when rendered dimensionless upon division by a regularization length, are interpreted as order parameters in the context of phase field theory. Dependence of the metric on internal state permits changes in lengths, areas, and volumes of material in conjunction with microstructure evolution. For example, voids may lead to dilatation, or structure collapse in B_4C may lead to densification [Clayton (2012); An and Goddard (2015)]. Incorporation of this metric tensor in the theory leads to a rescaled energy density and augmented balance laws that enable additional physics (e.g., pressure-shear coupling) without prescription of ad-hoc kinetic equations. The phase field-related components of the model are based on theory in Clayton et al. [Clayton and Knap (2011, 2014, 2016)], while the Finsler-geometric concepts entering the theory follow from Clayton [Clayton (2017b,c,a, 2018a)]. Potential advantages of the present computational implementation over other methods [Tomar, Zhai and Zhou (2004); Clayton (2005, 2009); Bammann and Solanki (2010)] for modeling inelasticity and fracture include the following: intrinsic regularization by gradient-dependent energy, little if any calibration of parameters, and preservation of mesh topology, e.g., no element deletion or separation

along element boundaries.

A recent study by Clayton et al. [Clayton, Leavy and Knap (2019)] invoked a simpler version of the present theory towards study of the same two ceramic composites. That work invoked pure phase field mechanics [Clayton and Knap (2016)] without incorporation of the pseudo-Finsler metric. Furthermore, uniaxial compression loading was simulated in Clayton et al. [Clayton, Leavy and Knap (2019)], while pure shear (i.e., biaxial tension-compression) is simulated in the present study. Shear strength is of high interest as it is thought to be an indicator of resistance to ballistic penetration in armor ceramics [Bourne (2008); Clayton (2015, 2016)].

Remaining sections of this work are organized as follows. The continuum theory and aspects of its computer implementation are reviewed in §2. Polycrystalline simulations, with results from shear loading, on B_4C-TiB_2 are given in §3. Parallel treatment of diamond-SiC is contained in §4, followed by conclusions.

2 Finsler-geometric phase field theory

The continuum theory invoked in subsequent simulations is tersely summarized here. The present approach extends that of Clayton et al. [Clayton, Leavy and Knap (2019)] to include a generalized pseudo-Finsler metric tensor [Clayton (2017c)], rather than the Euclidean (and more specifically, rectangular Cartesian) metric invoked in Clayton et al. [Clayton, Leavy and Knap (2019)]. The present theory implements linearized kinematics [Clayton and Knap (2015)] and quasi-static balance laws following from a variational approach [Clayton (2017b)]. Geometrically nonlinear and dynamic models are discussed elsewhere [Clayton (2017a); Clayton and Knap (2018a)].

2.1 Internal state

A vector $\boldsymbol{D}$ of internal state variables coincides with a director vector of Finsler geometry, though here this state vector need not be of unit length. Let $\boldsymbol{X}$ with Cartesian components X_K denote the reference position vector of a material particle. In a preferred coordinate system,

$$\boldsymbol{D}(\boldsymbol{X}) = \begin{bmatrix} D_1(\boldsymbol{X}) \\ D_2(\boldsymbol{X}) \\ D_3(\boldsymbol{X}) \end{bmatrix} = l \begin{bmatrix} \xi(\boldsymbol{X}) \\ \eta(\boldsymbol{X}) \\ 0 \end{bmatrix}. \tag{1}$$

Entries of $\boldsymbol{D}$ normalized by regularization length l are order parameters ξ and η. Parameter $\xi \in [0, 1]$ depicts fracture:

$$\xi(\boldsymbol{X}) = 0 \forall \boldsymbol{X} \in \text{ undamaged material,}$$
$$\xi(\boldsymbol{X}) \in (0, 1) \forall \boldsymbol{X} \in \text{ partially degraded material,} \tag{2}$$
$$\xi(\boldsymbol{X}) = 1 \forall \boldsymbol{X} \text{ fully failed material.}$$

Other structure changes are captured by $\eta \in [0,1]$:

$\eta(\boldsymbol{X}) = 0 \forall \boldsymbol{X} \in$ parent elastic crystal,

$\eta(\boldsymbol{X}) \in (0,1) \forall \boldsymbol{X} \in$ structural boundary zone,   (3)

$\eta(\boldsymbol{X}) = 1 \forall \boldsymbol{X} \in$ structurally transformed state.

For ceramics considered herein, $\eta > 0$ can track shearing by slip or twinning dislocations and monitor localized slip in amorphous bands. It also can represent density variations due to phase changes.

Metric tensor $\boldsymbol{G}$ depends potentially on coordinates $\boldsymbol{X}$ as well as internal state $\boldsymbol{D}$. Homogeneity is not required in the present generalized pseudo-Finsler theory [Bejancu (1990)], in contrast to strictly Finsler theories wherein only the direction of $\boldsymbol{D}$ is important. Though more general representations are admissible [Clayton (2017c)], the current model invokes Weyl-type isotropic scaling of the Cartesian metric $\boldsymbol{1}$, i.e., a conformal transformation [Clayton (2017b); Clayton and Knap (2018a)]:

$$\boldsymbol{G}(\xi, \eta) = \exp\left[\tfrac{1}{3}(m\xi^2 + k\eta^2)\right] \boldsymbol{1}.$$ (4)

Explicit dependence on $\boldsymbol{X}$ is not necessary for rectangular coordinates. Constants m and k quantify volume changes associated with respective fracture/cavitation and phase changes. The determinant is $G = \det \boldsymbol{G} = \exp(m\xi^2 + k\eta^2)$.

2.2 Kinematics

Displacement is $\boldsymbol{u} = \boldsymbol{u}(\boldsymbol{X})$. Let $\nabla(\cdot)$ denote the covariant derivative with respect to $\boldsymbol{X}$, here a partial coordinate derivative. Displacement gradient is decomposed as

$$\nabla \boldsymbol{u}(\boldsymbol{X}) = \boldsymbol{\beta}^E(\boldsymbol{X}) + \boldsymbol{\beta}^D[\xi(\boldsymbol{X}), \eta(\boldsymbol{X})].$$ (5)

Elastic distortion is $\boldsymbol{\beta}^E(\boldsymbol{X})$. The state-dependent contribution from changes in microstructure is [Clayton and Knap (2018a)]

$$\boldsymbol{\beta}^D(\xi, \eta) = x_\xi \phi_\xi(\xi)\boldsymbol{1} + x_\eta \phi_\eta(\eta)\boldsymbol{M} \otimes \boldsymbol{M} + \gamma_0 \phi_0(\eta)\boldsymbol{S} \otimes \boldsymbol{M}.$$ (6)

The first term on the right accounts for dilatation from cavitation or cracks, the second for compression or extension normal to a material plane from phase changes, the third for inelastic shearing. Vector $\boldsymbol{M}$ denotes the plane of structural transformations, slip, twinning, and/or localized shear, where the orthogonal shear direction is $\boldsymbol{S}$. Total strain is $\boldsymbol{\epsilon}$, and elastic strain is $\boldsymbol{\epsilon}^E$:

$$\boldsymbol{\epsilon} = \tfrac{1}{2}[\nabla \boldsymbol{u} + (\nabla \boldsymbol{u})^{\mathrm{T}}], \qquad \boldsymbol{\epsilon}^E = \tfrac{1}{2}[\boldsymbol{\beta}^E + (\boldsymbol{\beta}^E)^{\mathrm{T}}].$$ (7)

Polynomial interpolation functions in (6) are [Clayton, Leavy and Knap (2019)]

$$\phi_\xi(\xi) = 4\xi^3 - 3\xi^4, \quad \phi_\eta(\eta) = 4\eta^3 - 3\eta^4, \quad \phi_0(\eta) = 6\eta^2 - 8\eta^3 + 3\eta^4.$$ (8)

Damage deformation is idealized as isotropic with $x_\xi = \tfrac{1}{3}[\exp(\tfrac{m}{2}) - 1]$. Uniaxial strain normal to the basal plane commensurate with the phase change in B_4C [Clayton (2012, 2017c)] is quantified by $x_\eta = \exp(\tfrac{k}{2}) - 1$. Twinning on habit plane $\boldsymbol{M}$ is a simple shear whose maximum magnitude is γ_0. The same functions account for preferred single slip of full or partial dislocations along $\boldsymbol{S}$ with slip plane normal $\boldsymbol{M}$, where γ_0 is a saturation limit [Clayton (2018b)].

2.3 Energy functional and equilibrium equations

A total energy functional for a heterogeneous body Ω with boundary $\partial\Omega$ is

$$\begin{aligned}
\Psi(\boldsymbol{u}, \eta, \xi, \boldsymbol{X}) &= \int_\Omega [W(\nabla\boldsymbol{u}, \eta, \xi, \boldsymbol{X}) + f(\eta, \xi, \nabla\eta, \nabla\xi, \boldsymbol{X})]\mathrm{d}V \\
&= \int_\Omega [W(\nabla\boldsymbol{u}, \eta, \xi, \boldsymbol{X}) + f(\eta, \xi, \nabla\eta, \nabla\xi, \boldsymbol{X})]\sqrt{G(\eta, \xi)}\mathrm{d}V_0.
\end{aligned} \tag{9}$$

Strain energy per unit volume is W, phase energy is f, and their sum is $\psi = W + f$. In a reference state of pseudo-Finsler space, a volume element of the body is scaled as $\mathrm{d}V = \sqrt{G}\mathrm{d}V_0$, where $\mathrm{d}V_0$ is the element in Cartesian space. Properties may vary with $\boldsymbol{X}$, e.g., among grains in a polycrystal. Position $\boldsymbol{X}$ is dropped from the explicit list of arguments in subsequent derivations, where it is understood that properties are homogeneous within each sub-volume of a grain [Clayton and Knap (2016)].

Internal state contributions, including gradient effects, are embedded in function f:

$$f(\eta, \xi, \nabla\eta, \nabla\xi) = f_0(\eta, \xi) + g_0(\xi) + f_1(\xi, \nabla\eta) + g_1(\nabla\xi); \tag{10}$$

$$\begin{aligned}
f_1(\xi, \nabla\eta) &= \boldsymbol{\kappa}(\xi) : (\nabla\eta \otimes \nabla\eta), \qquad \boldsymbol{\kappa}(\xi) = \kappa_0 \hat{\imath}(\xi)\boldsymbol{1}, \\
g_1(\nabla\xi) &= \boldsymbol{\omega} : (\nabla\xi \otimes \nabla\xi), \qquad \boldsymbol{\omega} = \omega_0[\boldsymbol{1} + \hat{\beta}(\boldsymbol{1} - \boldsymbol{N} \otimes \boldsymbol{N})].
\end{aligned} \tag{11}$$

Function $\hat{\imath}(\xi) = \zeta + (1 - \zeta)(1 - \xi)^2$, with ζ a constant subject to $0 < \zeta \ll 1$. Anisotropic fracture results from setting $\hat{\beta} > 0$.

Denote the mechanical traction vector by $\boldsymbol{t}$, the conjugate surface force to η by r, and the conjugate surface force to ξ by s. Stationary points of $\Psi = \int \psi \mathrm{d}\Omega$ are solutions to the following variational equation at fixed $\boldsymbol{X}$:

$$\delta\Psi = \oint_{\partial\Omega} (\boldsymbol{t} \cdot \delta\boldsymbol{u} + r\delta\eta + s\delta\xi)\mathrm{d}S. \tag{12}$$

Euler-Lagrange equations resulting from this principle and application of Rund's divergence theorem [Rund (1975)] are the static balance of linear momentum

$$\nabla \cdot \frac{\partial W}{\partial \nabla\boldsymbol{u}} = -(m\xi\nabla\xi + k\eta\nabla\eta) \cdot \frac{\partial W}{\partial \nabla\boldsymbol{u}}, \tag{13}$$

and the static equilibrium equations for internal state:

$$\begin{aligned}
\frac{\partial f}{\partial \eta} + \frac{\partial W}{\partial \eta} - 2\nabla \cdot (\boldsymbol{\kappa}\nabla\eta) &= 2[\boldsymbol{\kappa}\nabla\eta \cdot (m\xi\nabla\xi + k\eta\nabla\eta) - k\eta\psi], \\
\frac{\partial f}{\partial \xi} + \frac{\partial W}{\partial \xi} - 2\nabla \cdot (\boldsymbol{\omega}\nabla\xi) &= 2[\boldsymbol{\omega}\nabla\xi \cdot (m\xi\nabla\xi + k\eta\nabla\eta) - m\xi\psi].
\end{aligned} \tag{14}$$

Right sides of (13) and (14) vanish identically for a Riemannian metric ($m = k = 0$) and in such cases coincide with phase field mechanics [Clayton and Knap (2016); Clayton, Leavy and Knap (2019)]. Stress $\boldsymbol{P}$ is symmetric:

$$\boldsymbol{P} = \frac{\partial W}{\partial \boldsymbol{\epsilon}} = \frac{\partial W}{\partial \nabla\boldsymbol{u}}. \tag{15}$$

Natural boundary conditions on $\partial\Omega$ with outward unit normal $\boldsymbol{n}$ are

$$\boldsymbol{t} = \boldsymbol{P} \cdot \boldsymbol{n}, \qquad r = 2\boldsymbol{\kappa} : (\nabla\eta \otimes \boldsymbol{n}), \qquad s = 2\boldsymbol{\omega} : (\nabla\xi \otimes \boldsymbol{n}). \tag{16}$$

Strain energy density is linear elastic with damage-dependent moduli λ, μ, K:

$$W = \tfrac{1}{2}\lambda(\mathrm{tr}\boldsymbol{\epsilon}^E)^2 + \mu\boldsymbol{\epsilon}^E : \boldsymbol{\epsilon}^E; \tag{17}$$

$$\mu(\xi) = \mu_0[\zeta + (1-\zeta)(1-\xi)^2], \qquad \lambda(\xi, \mathrm{tr}\boldsymbol{\epsilon}^E) = K(\xi, \mathrm{tr}\boldsymbol{\epsilon}^E) - \tfrac{2}{3}\mu(\xi); \tag{18}$$

$$K(\xi, \mathrm{tr}\boldsymbol{\epsilon}^E) = (\lambda_0 + \tfrac{2}{3}\mu_0)\{[\zeta + (1-\zeta)(1-\xi)^2]\langle\mathrm{tr}\boldsymbol{\epsilon}^E\rangle + \langle-\mathrm{tr}\boldsymbol{\epsilon}^E\rangle^*\}; \tag{19}$$

where $\langle x\rangle = 1\forall x > 0$, $\langle x\rangle = 0\forall x \leq 0$, $\langle x\rangle^* = 1\forall x \geq 0$, and $\langle x\rangle^* = 0\forall x < 0$. Accordingly, tangent elastic moduli μ and λ reduce in magnitude as ξ increases. Minimum values are $\zeta\mu_0$ and $\zeta\lambda_0$ when $\xi(\boldsymbol{X}) = 1$, corresponding to complete local fracture at $\boldsymbol{X}$. In the numerical implementation, elements whose nodes contain values of ξ at or approaching unity are considered fractured, but these elements are never removed from the simulation since they contain a very small yet finite stiffness to prevent interpenetration. According to (19), the bulk modulus retains its full initial value $K_0 = \lambda_0 + \tfrac{2}{3}\mu_0$ for compressive elastic volume changes such that unrealistic local collapse of the material is prohibited. Thus, under compressive pressure, behavior of the material becomes akin to that of a compressible elastic fluid. This approach of addressing failed elements is standard in phase field simulations of fracture [Borden, Verhoosel, Scott et al. (2012); Clayton and Knap (2014)].

Gradient-independent energy functions in (10) are, with $\mathrm{H}(\cdot)$ a Heaviside function,

$$f_0(\eta, \xi) = [A\eta^2(\eta_0 - \eta)^2\mathrm{H}(\eta_0 - \eta) + \hat{A}\eta^2]\hat{\iota}(\xi), \qquad g_0(\xi) = B\xi^2. \tag{20}$$

The first term in f_0 is a double-well with minima at $\eta = (0, \eta_0)$, a local maximum at $\eta = \eta_0/2$, and a cut-off $\eta_0 > 0$. Quadratic forms are the remainder of f_0 and g_0. Constants entering (20) are A, η_0, $\hat{A}$, and B. Let Γ denote twin boundary or stacking fault energy, Υ fracture surface energy. Material constants are related by

$$A = 12\frac{\Gamma}{\eta_0^4 l}, \quad \kappa_0 = \frac{3}{4}\frac{\Gamma l}{\eta_0^2}; \qquad B = \frac{\Upsilon}{l}, \qquad \omega_0 = \Upsilon l. \tag{21}$$

Constant $\hat{A}$ is an energy barrier for phase changes and can also account for energy of dislocation lines. Valuess for each crystal type follow later in §3 and §4.

2.4 Numerical methods

The FE method is used to solve 3D problems in an incremental fashion. Boundary conditions are updated at each load increment. Numerical algorithms apply conjugate gradient energy minimization [Clayton and Knap (2016)]. Solution fields $\boldsymbol{u}(\boldsymbol{X}), \eta(\boldsymbol{X}), \xi(\boldsymbol{X})$ minimize Ψ subject to boundary constraints, where the second of (9) is used. In this context, V_0 is the volume of the FE domain in its initial undeformed state in Euclidean space, prior to structural transformations. Force residuals computed numerically from Ψ must be smaller than a prescribed tolerance; (13) and (14) are not evaluated explicitly. Irreversibility is

ensured by constraints $\delta\xi(\boldsymbol{X}) \geq 0$ for $\xi(\boldsymbol{X}) \geq \xi_T$ and $\delta\eta(\boldsymbol{X}) \geq 0$ for $\eta(\boldsymbol{X}) \geq \eta_T$, where $\xi_T = \eta_T = 0.9$. According to the present variational model based on energy minimization similar to Bourdin et al. [Bourdin, Francfort and Marigo (2000)], strain rate does not influence the results, which are effectively time-independent. Inertia and stress waves are excluded, as are kinetics of internal state that can be addressed using methods described elsewhere [Clayton and Knap (2018a)].

3 Boron carbide-titanium diboride polycrystals

Properties and FE renderings of B_4C-TiB_2 are presented, followed by numerical results for pure shear loading.

3.1 Material representation

Material properties and FE models are discussed in brief, noting that detailed justification and sources of property data are available in Clayton et al. [Clayton, Leavy and Knap (2019)]. Parameters entering models of B_4C and TiB_2 are summarized in Tab. 1.

First consider B_4C. Twinning occurs on $\langle 10\bar{1}0\rangle\{0001\}$ and fracture on $\{0001\}$. Amorphous shear bands can form inside twins. Twinning shear is γ_0, and twinning surface energy is Γ. Lattice collapse normal to (0001) produces x_η, and x_ξ measures expansion from cavitation [An and Goddard (2015)]. The crystal-to-glass energy barrier is $\hat{A}$. Fracture energy is Υ and cleavage anisotropy is $\hat{\beta}$.

Now consider TiB_2. Fracture occurs on $\{0001\}$, with Υ the surface energy [Du and Chen (2018)]. Order parameter η addresses stacking fault energy and line energy of (partial) dislocations via A and $\hat{A}$, respectively. Dilatation from fractures is represented by $x_\xi > 0$. Denote the Burgers vector of a partial dislocation by b, cumulative dislocation density by ρ_D. The lowest energy barrier corresponds to $\langle 11\bar{2}0\rangle\{0001\}$ slip [Du and Chen (2018)]. Stacking fault energy Γ is inferred from Vanderwalker et al. [Vanderwalker and Croft (1988)]. Let $\bar{x}$ denote the maximum distance a (partial) dislocation travels prior to arrest. Let ρ_S denote the saturation dislocation density. Stored line energy is $\frac{1}{2}\mu_0 b^2 \rho_D$ [Clayton (2011)], with full Burgers vector b_0. The phase field representation of single partial slip in TiB_2 thus obeys

$$\eta = (b/b_0)\sqrt{\rho_D/\rho_S}, \qquad \gamma_0 = \rho_S b_0 \bar{x}, \qquad \hat{A} = \tfrac{1}{2}\mu_0 b_0^2 \rho_S. \qquad (22)$$

Residual stresses may affect toughness [White and Dickey (2011); Scharf and Rubink (2018)]. These may be addressed in future work along with other defects.

Domains consist of 50 crystal polyhedra comprising a cube Ω of edge length $L = 10\,\mu$m. Average grain size is $L/50^{1/3} \approx 2.5\,\mu$m. Numerals 1 and 2 pertain to B_4C and TiB_2, respectively. Morphologies with volume fractions V_2 of 10% and 18% are simulated. These are shown in Fig. 1. Volume fractions are physically comparable to those of real microstructures [Scharf and Rubink (2018)]. Two random orientation distributions $(\boldsymbol{S}, \boldsymbol{M}, \boldsymbol{N})$ are assigned to grain lattices of each morphology, such that four simulations are reported in total.

Table 1: Material constants for B_4C and TiB_2 [Clayton, Leavy and Knap (2019)]

Parameter [units]	Definition	Value - B_4C	Value - TiB_2
μ_0 [GPa]	initial shear modulus	193	249
λ_0 [GPa]	initial Lamé modulus	108	27
Υ [J/m^2]	fracture energy	3.27	4.14
Γ [J/m^2]	twin boundary or SF energy	0.54	0.12
$\hat{\beta}$	fracture anisotropy	100	100
l [μm]	regularization length	0.1	0.1
γ_0	max twin shear or plastic slip	0.31	0.015
η_0	cut-off for double-well energy	0.68	0.68
$\hat{A}$ [MPa]	phase or dislocation energy	188	11.4
x_η, x_ξ	phase densification, cavitation	-0.04, 0.013	0, 0.013
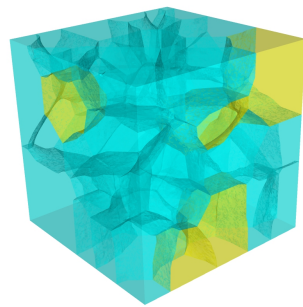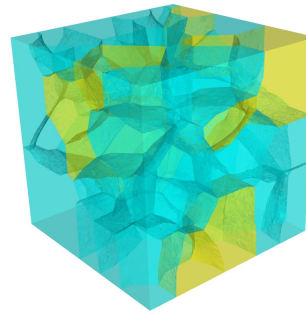
(a) microstructure 1   (b) microstructure 2

Figure 1: FE meshes; (B_4C, TiB_2) crystals are (teal, yellow) and V_2 is the volume fraction of TiB_2: (a) microstructure 1, $V_2 = 0.10$ (b) microstructure 2, $V_2 = 0.18$

Displacement-controlled boundary conditions on part of $\partial\Omega$ correspond to pure shear [Clayton and Knap (2018b)], consisting of tension and compression applied in equal magnitudes along perpendicular Y- and Z-directions. Let $\bar{\epsilon}$ denote the load parameter. Essential boundary conditions are applied to four of the six faces of the initially cube-shaped polycrystalline aggregate:

$$u_Y(X, 0, Z) = 0, \quad u_Y(X, L, Z) = \bar{\epsilon}L; \quad u_Z(X, Y, 0) = 0, \quad u_Z(X, Y, L) = -\bar{\epsilon}L. \quad (23)$$

Along the remaining two faces of the domain ($X = 0, X = L$), traction-free conditions allow the body to expand or contract freely in the X-direction. Regarding conjugate forces to internal state, free boundary conditions $r = s = 0$ on all of $\partial\Omega$. In the current implementation of these boundary conditions, average shear strain $\bar{\epsilon}$ is increased incrementally in steps of 5×10^{-4}. Conjugate gradient energy minimization [Clayton and Knap (2016)] is used to seek an equilibrium configuration of the body at each increment.

3.2 Computational results

Microstructures for grains of lattice orientation set 1 are shown in Fig. 2 at an applied shear strain of $\bar{\epsilon} = 0.01 = 1\%$. Order parameter η denotes twinning, shear localization, and amorphization in the B_4C phase and basal slip in the TiB_2 phase. A quadratic scale is used to visualize low transformation magnitudes ($0 \lesssim \eta \lesssim 0.25$). Elements with $\xi > 0.8$ are visually removed to show fractures. As explained following (18) and (19), such elements possess very low tangent stiffness, with $\mu \to \zeta\mu_0$ as $\xi \to 1$ in shear for example, where herein $\zeta = 0.01$. These elements are never fully removed from the calculation; original mesh topology is retained.

Fracture paths are quite similar for microstructures 1 and 2 in respective Fig. 2(a) and Fig. 2(b). Cleavage cracks tend to traverse the more brittle B_4C grains. Transformation behaviors ($\eta > 0$) are enhanced in microstructure 2 relative to microstructure 1, notably in grains of the TiB_2 phase which have a lower stacking fault energy (0.12 versus 0.54 J/m^2) and thus a lower resistance to slip than the twinning threshold of B_4C. In both of these cases, and in others not shown in Fig. 2 for orientation set 2, inelasticity mechanisms of slip, twinning, and amorphization are relatively scarce ($\eta \ll 1$ in most grains), in agreement with experimental observations from samples of comparable sizes [Clayton and Knap (2018a); Scharf and Rubink (2018)].

Volume-averaged maximum shear stress and order parameters are labeled $\bar{P}$, $\bar{\eta}$, and $\bar{\xi}$, respectively. Definitions of the latter two are obvious, while the stress averaged over the reference domain is

$$\bar{P} = \tfrac{1}{2} \int_\Omega |P_{YY} - P_{ZZ}|\sqrt{G}\mathrm{d}V_0. \quad (24)$$

Values are shown versus applied shear strain $\bar{\epsilon}$ in Fig. 3. Average stresses in Fig. 3(a) demonstrate modest effects of lattice orientation and volume fractions, recalling microstructure 1 *vs.* 2 in Fig. 1 with 10% and 18% TiB_2, respectively. Stiffer responses are obtained for the same lattice orientation set when the fraction of TiB_2 is increased.
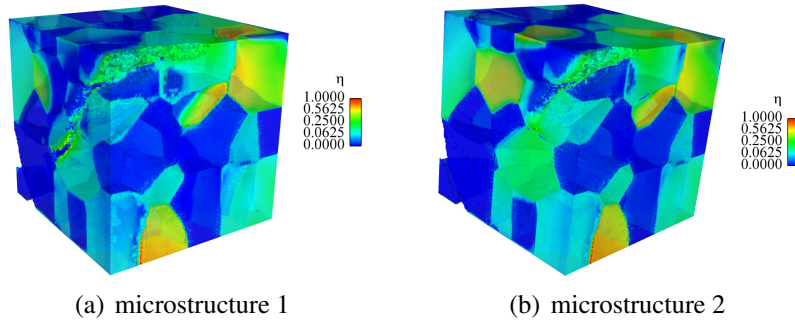
(a) microstructure 1   (b) microstructure 2

Figure 2: B$_4$C-TiB$_2$, lattice 1, shear strain $\bar{\epsilon} = 1\%$: (a) $V_2 = 0.10$ (b) $V_2 = 0.18$

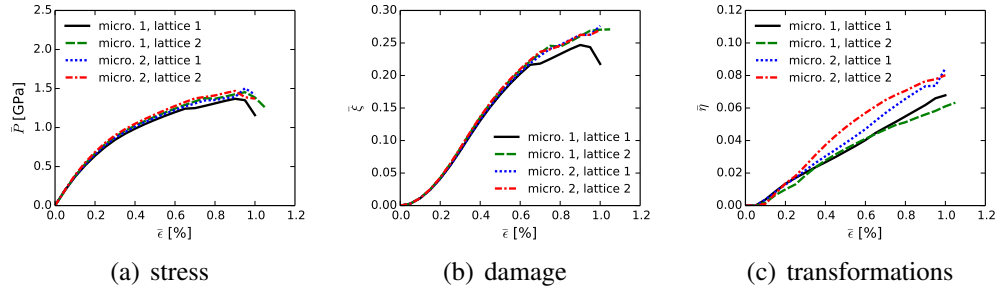(a) stress   (b) damage   (c) transformations

Figure 3: Averaged results for B$_4$C-TiB$_2$ versus applied shear strain $\bar{\epsilon}$: (a) shear stress $\bar{P}$ (b) fracture $\bar{\xi}$ (c) twinning, phase change, or slip $\bar{\eta}$

This results from the higher elastic shear modulus of TiB$_2$ as well this phase's higher fracture energy, greater ductility due to slip, and lower tendency to cleave (Tab. 1). Average damage $\bar{\xi}$ in Fig. 3(b) evolves similarly for all cases except microstructure 1 with lattice 1. Interestingly, this is the structurally weakest case in terms of average shear stress, yet it demonstrates the lowest accumulation rate of average micro-crack density. The same trend has been observed in simulations of pure B$_4$C [Clayton and Knap (2018a,b)]: overall stiffness reduction and failure are most closely correlated with the presence of a few dominant cracks and are inversely correlated with diffuse crack density. Average structural changes are reported in Fig. 3(c). Microstructure 2 demonstrates more inelasticity than microstructure 1 since the former contains more TiB$_2$ that slips more easily than shear-induced inelastic modes (twinning and localization) in B$_4$C.

Tab. 2 lists average maximum shear stress and values of applied shear strain and averaged order parameters at the same peak loading increment. Peak stress P_C increases from 1% to 10% when the volume fraction of TiB$_2$ is increased from 10% to 18%. Transformations η_C increase with V_2 for reasons outlined in the context of Fig. 3(c). Trends are less obvious for ductility ϵ_C and peak damage ξ_C. Different trends are evident in these variables for

Table 2: Peak shear stress (P_C), associated strain (ϵ_C), and averaged order parameters (ξ_C, η_C) for B_4C-TiB_2

Microstructure (fraction TiB_2)	Lattice orientation	P_C [GPa]	ϵ_C [%]	ξ_C	η_C
1 ($V_2 = 0.10$)	1	1.37	0.90	0.247	0.062
	2	1.46	0.95	0.271	0.058
2 ($V_2 = 0.18$)	1	1.51	0.95	0.263	0.074
	2	1.47	0.90	0.262	0.077

lattice 1 and lattice 2. Lattice orientation affects overall ductility and damage via the action of resolved driving forces for inelasticity and fracture that depend on orientations of basal planes for slip, twinning, and cleavage. Differences due to lattice orientation can be comparable in magnitude to differences due to volume fraction of the second phase.

Experiments suggest fracture toughness of polycrystalline B_4C may be improved by 10-100% and flexure strength by 10-30% via addition of 13-23% TiB_2 [Scharf and Rubink (2018)]. The current simulations show more modest improvements with increasing TiB_2. Residual stresses omitted in the simulations may partially explain the discrepancy. Since the FE domain may not be large enough to capture long-crack blunting by TiB_2, it may be enlarged to include more crystals in the future.

4 Diamond-silicon carbide polycrystals

Properties and FE representations for diamond (C)-β-SiC are reported, followed by simulation results for pure shear loading.

4.1 Material representation

Model features for each crystal type are summarized briefly here; details and supporting references can be found in Clayton et al. [Clayton, Leavy and Knap (2019)]. Properties are given in Tab. 3. First consider diamond. Cleavage occurs on $\{111\}$, with surface energy Υ. Dilatation from crack opening is quantified by $x_\xi > 0$, with the same value used for all ceramics of present interest. Silicon carbide can fracture and twin. Cleavage planes are $\{110\}$. Twinning in the zinc blende structure occurs on $\langle 11\bar{2}\rangle\{111\}$ with $\gamma_0 = \sqrt{2}/2$ [Van Torne (1966)]. Stacking fault energy Γ is notably low [Ning and Ye (1990)]. Regularization length l is universal among all ceramics addressed. As in §3, residual stresses and other microstructure heterogeneities (initial pores, tertiary phases, etc.) are deferred to future work.

Two very different morphologies are modeled, as shown in Fig. 4. Both domains are cubes of the same dimensions of §3, containing 50 polyhedral grains of average size $L/50^{1/3} \approx 2.5\,\mu$m. Denote by V_1 and V_2 volume fractions of diamond and SiC phases, respectively. Microstructure 1 features a layer of uniform thickness (200 nm) of nano-crystalline SiC fully surrounding each diamond crystal, contributing $V_2 = 20\%$. Microstructure 2 contains

Table 3: Material constants for C and SiC [Clayton, Leavy and Knap (2019)]

Parameter [units]	Definition	Value - C	Value - SiC
μ_0 [GPa]	initial shear modulus	553	203
λ_0 [GPa]	initial Lamé modulus	73	90
Υ [J/m^2]	fracture energy	5.30	1.70
Γ [J/m^2]	twin boundary or SF energy	-	0.034
$\hat{\beta}$	fracture anisotropy	100	100
l [μm]	regularization length	0.1	0.1
γ_0	max twin shear or plastic slip	-	0.707

(a) microstructure 1   (b) microstructure 2
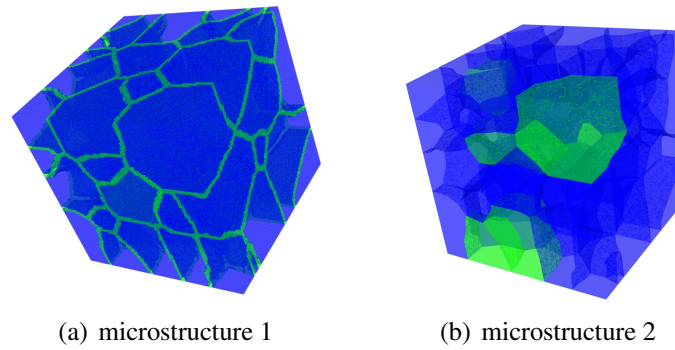
Figure 4: FE meshes; (C, SiC) crystals are (blue, green) and V_2 is the volume fraction of SiC: (a) microstructure 1, $V_2 = 0.20$ (b) microstructure 2, $V_2 = 0.10$

five bulk SiC grains contributing $V_2 = 10\%$. Two possible random lattice orientation sets give $(\boldsymbol{S}, \boldsymbol{M}, \boldsymbol{N})$ for the 50 grains.

A uniform orientation for nanocrystalline SiC layer is used in microstructure 1: boundary layer grains are too small to be resolved by the FE mesh. A $\{110\}$ potential fracture plane is oriented at $45°$ to the direction of compression-tension, providing a maximum resolved stress for shear fracture. If loading is normal to [010] (tension) and [001] (compression), the active twinning system for $(\boldsymbol{S}, \boldsymbol{M})$ is $[11\bar{2}](111)$, and $\boldsymbol{N}$ is prescribed as (101) for orientation set 1 and $(0\bar{1}1)$ for set 2.

Boundary conditions for pure shear are prescribed nearly identically to those discussed in §3. For each of the two orientation sets with microstructure 1, one simulation is performed with boundary conditions of (23) and $\bar{\epsilon} \geq 0$, and a second with the sign of $\bar{\epsilon}$ reversed. In the forthcoming discussion of results of each of these second simulations, $\bar{\epsilon}$ refers to the magnitude of (negative) applied shear strain for ease of comparison. Twinning in the nanocrystalline layer is promoted in the former case but precluded in the latter since the driving force, i.e., resolved shear stress for twinning, becomes negative. For microstructure 2, $\bar{\epsilon} \geq 0$ only. The total number of simulations reported in §4 is six.

4.2 Finite element simulations and analysis of results

Shown in Fig. 5 are contours of η that show twinning in the SiC phase. Results correspond to lattice orientation set 1, where the habit plane and twinning direction are oriented to promote twinning in the nano-crystalline grain boundary (GB) layer in Fig. 5(a). Quadratic scales enable visualization of low to moderate, i.e., incomplete, twinning ($0 \lesssim \eta \lesssim 0.25$) that occurs in this GB layer and in a few preferentially oriented bulk grains of SiC in Fig. 5(b). Physically, incomplete twinning corresponds to planar stacking faults typical in β-SiC. Diamond, which comprises the majority of each microstructure, does not undergo twinning or slip, so $\eta = 0$ in all diamond crystals. Fracture behaviors are notably different for the two cases shown, where cleavage cracks in the diamond grains are evident at different locations in each microstructure. A dominant cleavage crack cutting diagonally across multiple diamond crystals through entire domain is noteworthy in microstructure 2, while smaller cracks arrested or deflected at phase boundaries are evident in microstructure 1. Intergranular fractures are more common in the latter microstructure.

Volume-averaged shear stress $\bar{P}$ is defined as in (24), and volume-averaged order parameters $\bar{\eta}$ and $\bar{\xi}$ are calculated similarly. Values are shown versus applied shear strain $\bar{\epsilon}$ in Fig. 6. Stresses for all six simulations of diamond-SiC are reported in Fig. 6(a). Recall that for two of the simulations with microstructure 1, the twin system in the GB phase is oriented with respect to the loading mode such that twinning is precluded. Lattice orientations of diamond grains are maintained identically with their counterparts in the legend immediately above. Initial elastic stiffness is larger in microstructure 2, which has a lower volume fraction than microstructure 1 ($V_2 = 0.10$ *vs.* 0.20) of the elastically stiffer diamond phase. However, maximum stresses are often lower for microstructure 2 and always occur at a lower applied strain for microstructure 1. When twinning is suppressed in microstructure 1, effective stiffness increases since local deformation in the GB phase remains elastic until fracture. No trends are discernible for behaviors in the strain softening regime, which differ substantially among microstructures and orientations. The same can be inferred with regard to average damage $\bar{\xi}$ in Fig. 6(b), and correlations with average stress are not all obvious. The rate of damage accumulation does decrease, however, at strains beyond those corresponding to maximum average stress. Transformation behavior quantified in Fig. 6(c) is logically explained. Microstructure 1 demonstrates significant activity due to the preferential orientation of its twinning system in the nano-crystalline GB layers. Minor transformation behavior is reflected by $\bar{\eta}$ for microstructure 2 as a result of twinning in a few bulk grains, e.g., see Fig. 5(b). When twinning is suppressed in microstructure 1, $\bar{\eta} \to 0$ since the diamond phase is elastic-brittle.

Tabulated results for peak shear stress, corresponding ductility or peak strain, and order parameters are found in Tab. 4. Peak shear stress P_C decreases by up to 10% when the GB phase is able to twin in microstructure 1, while ductility is about the same or slightly improved with twinning. Compared to microstructure 1 which contains half as much of the weaker SiC phase by volume (10% versus 20%), microstructure 2 demonstrates lower peak shear stress than three of the four simulations with microstructure 1. Ductility $\bar{\epsilon}_C$ is
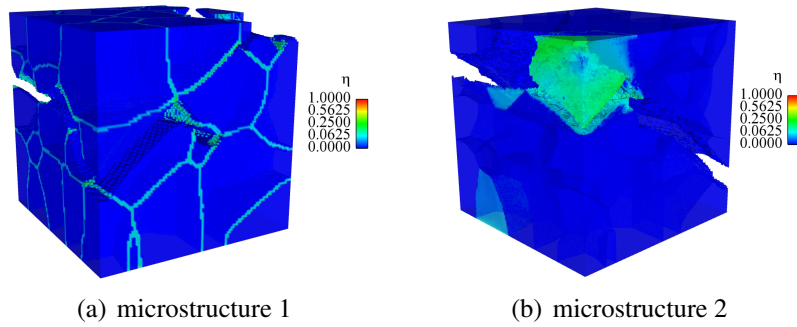
(a) microstructure 1   (b) microstructure 2

Figure 5: C-SiC, lattice 1, shear strain $\bar{\epsilon} = 0.9\%$: (a) $V_2 = 0.20$, (b) $V_2 = 0.10$

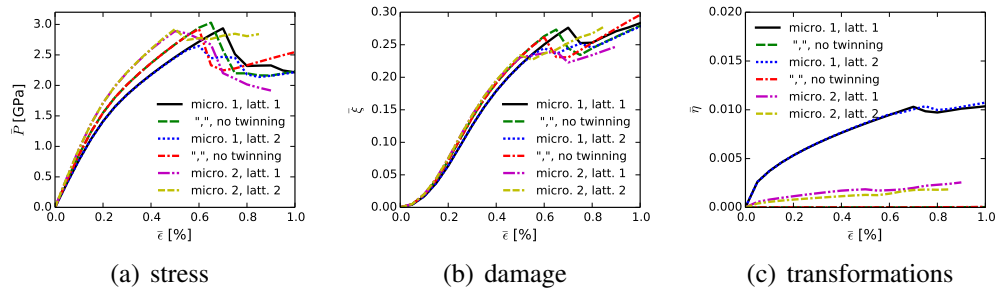(a) stress   (b) damage   (c) transformations

Figure 6: Averaged results for diamond-SiC versus applied shear strain $\bar{\epsilon}$: (a) shear stress $\bar{P}$ (b) fracture $\bar{\bar{\xi}}$ (c) twinning $\bar{\eta}$

Table 4: Peak shear stress (P_C), associated strain (ϵ_C), and averaged order parameters (ξ_C, η_C) for C-SiC composites

Microstructure (fraction SiC)	Lattice orientation	Slip/twins active	P_C [GPa]	ϵ_C [%]	ξ_C	η_C
1 ($V_2 = 0.20$)	1	Y	2.94	0.70	0.276	0.0101
	2	Y	2.65	0.60	0.245	0.0095
	1	N	3.03	0.65	0.273	-
	2	N	2.93	0.60	0.262	-
2 ($V_2 = 0.10$)	1	Y	2.89	0.50	0.231	0.0019
	2	Y	2.92	0.50	0.234	0.0013

lowered by 15 to 30% in microstructure 2 compared to microstructure 1. Transformation measured by η_C is much larger in microstructure 1 (when twinning is enabled) than 2 since it contains a larger percentage of SiC preferentially oriented for twinning. Peak damage ξ_C is lower in microstructure 2 than 1, suggesting dominant cracks in the former and diffuse damage in the latter, more durable aggregates. The present findings agree qualitatively with experiments [Zhao, Qian, Daemen et al. (2004)]: fracture toughness of polycrystalline diamond is improved by intergranular nano-crystalline SiC layers.

As was also the case for B_4C-TiB_2 reported in §3, trends in results for diamond-SiC depend on lattice orientation. In the present material, fracture is strongly affected by orientation of octahedral cleavage planes in the diamond phase, and ductility by orientations of twinning habit planes in the SiC phase. As an exception to other trends implied already, for lattice 2 with slip/twins active, P_C is lower in microstructure 1 than microstructure 2. Differences in strength between microstructures due to phase volume fractions and interface morphology depend strongly on enabling of twinning activity or lack thereof. This suggests important coupling exists among mechanisms of twinning, interfacial failure, and cleavage fracture.

5 Conclusions

A constitutive theory incorporating ideas from Finsler differential geometry and phase field mechanics has been implemented to model deformation and failure of dual-phase ceramics under pure shear loading. Simulations of polycrystalline B_4C-TiB_2 and diamond-SiC composites demonstrate different twinning, amorphization, slip, and fracture behaviors of these ceramics depending on crystal type, lattice orientation, and phase morphology. Addition of TiB_2 to B_4C provides an increase in overall shear strength and ductility, where the former phase is more likely to shear inelastically and possesses a higher fracture energy, thereby enabling blunting of cleavage cracks initiated in the more brittle B_4C phase. The SiC phase, when incorporated as nano-crystalline layers along grain boundaries, apparently obstructs paths of cleavage cracks in brittle diamond crystals. For improved failure resistance, encapsulation of diamond in very fine grains of the softer second phase is recommended over addition of SiC grains of commensurate size of the diamond. For quasi-static deformations of aggregates of 50 bulk crystals with grain sizes on the order of several μm, maximum shear strengths are on the order of 1.5 GPa for B_4C-TiB_2 and 2.9 GPa for diamond-SiC. Respective applied shear strains at maximum load are on the order of 0.9% and 0.6% for the two material systems.

References

An, Q.; Goddard, W. (2015): Atomistic origin of brittle failure of boron carbide from large-scale reactive dynamics simulations: suggestions toward improved ductility. *Physical Review Letters*, vol. 115, pp. 105051.

Bammann, D.; Solanki, K. (2010): On kinematic, thermodynamic, and kinetic coupling of a damage theory for polycrystalline material. *International Journal of Plasticity*, vol. 26, pp. 775-793.

Bejancu, A. (1990): *Finsler Geometry and Applications*. Ellis Horwood, New York.

Borden, M.; Verhoosel, C.; Scott, M.; Hughes, T.; Landis, C. (2012): A phase-field description of dynamic brittle fracture. *Computer Methods in Applied Mechanics and Engineering*, vol. 217, pp. 77-95.

Bourdin, B.; Francfort, G.; Marigo, J. J. (2000): Numerical experiments in revisited brittle fracture. *Journal of the Mechanics and Physics of Solids*, vol. 48, pp. 797-826.

Bourne, N. (2008): The relation of failure under 1D shock to the ballistic performance of brittle materials. *International Journal of Impact Engineering*, vol. 35, pp. 674-683.

Chen, M.; McCauley, J.; Hemker, K. (2003): Shock-induced localized amorphization in boron carbide. *Science*, vol. 299, pp. 1563-1566.

Clayton, J. (2005): Dynamic plasticity and fracture in high density polycrystals: constitutive modeling and numerical simulation. *Journal of the Mechanics and Physics of Solids*, vol. 53, pp. 261-301.

Clayton, J. (2009): A continuum description of nonlinear elasticity, slip and twinning, with application to sapphire. *Proceedings of the Royal Society of London A*, vol. 465, pp. 307-334.

Clayton, J. (2011): *Nonlinear Mechanics of Crystals*. Springer, Dordrecht.

Clayton, J. (2012): Towards a nonlinear elastic representation of finite compression and instability of boron carbide ceramic. *Philosophical Magazine*, vol. 92, pp. 2860-2893.

Clayton, J. (2015): Penetration resistance of armor ceramics: dimensional analysis and property correlations. *International Journal of Impact Engineering*, vol. 85, pp. 124-131.

Clayton, J. (2016): Dimensional analysis and extended hydrodynamic theory applied to long-rod penetration of ceramics. *Defence Technology*, vol. 12, pp. 334-342.

Clayton, J. (2017): Finser-geometric continuum dynamics and shock compression. *International Journal of Fracture*, vol. 208, pp. 53-78.

Clayton, J. (2017): Finsler geometry of nonlinear elastic solids with internal structure. *Journal of Geometry and Physics*, vol. 112, pp. 118-146.

Clayton, J. (2017): Generalized finsler geometric continuum physics with applications in fracture and phase transformations. *Zeitschrift fur Angewandte Mathematik und Physik*, vol. 68, pp. 9.

Clayton, J. (2018): Generalized pseudo-Finsler geometry applied to the nonlinear mechanics of torsion of crystalline solids. *International Journal of Geometric Methods in Modern Physics*, vol. 15.

Clayton, J. (2018): Shock compression of metal single crystals modeled via Finsler-geometric continuum theory. *AIP Conference Proceedings*, vol. 1979.

Clayton, J.; Knap, J. (2011): A phase field model of deformation twinning: nonlinear theory and numerical simulations. *Physica D*, vol. 240, pp. 841-858.

Clayton, J.; Knap, J. (2014): A geometrically nonlinear phase field theory of brittle fracture. *International Journal of Fracture*, vol. 189, pp. 139-148.

Clayton, J.; Knap, J. (2015): Phase field modeling of directional fracture in anisotropic polycrystals. *Computational Materials Science*, vol. 98, pp. 158-169.

Clayton, J.; Knap, J. (2016): Phase field modeling of coupled fracture and twinning in single crystals and polycrystals. *Computer Methods in Applied Mechanics and Engineering*, vol. 312, pp. 447-467.

Clayton, J.; Knap, J. (2018): Continuum modeling of twinning, amorphization, and fracture: theory and numerical simulations. *Continuum Mechanics and Thermodynamics*, vol. 30, pp. 421-455.

Clayton, J.; Knap, J. (2018): Geometric micromechanical modeling of structure changes, fracture, and grain boundary layers in polycrystals. *Journal of Micromechanics and Molecular Physics*, vol. 3, pp. 1840001.

Clayton, J.; Leavy, R.; Knap, J. (2019): Phase field m odeling o f heterogeneous microcrystalline ceramics. *International Journal of Solids and Structures*, vol. 166, pp. 183-196.

Du, J.; Chen, R. (2018): First principles calculations of interfacial structures and impact on mechanical properties in armor ceramics. *Technical Report W911NF-16-2-0189*. University of North Texas, Denton, TX.

Ning, X.; Ye, H. (1990): Experimental determination of the intrinsic stacking-fault energy of SiC crystals. *Journal of Physics: Condensed Matter*, vol. 2, pp. 10223-10225.

Rund, H. (1975): A divergence theorem for Finsler metrics. *Monatshefte fur Mathematik*, vol. 79, pp. 233-252.

Scharf, T.; Rubink, W. (2018): Development of high strength, high toughness B_4C-based composites. *Technical Report W911NF-16-2-0189*. University of North Texas, Denton, TX.

Sigl, L.; Kleebe, H. J. (1995): Microcracking in B_4C-TiB_2 composites. *Journal of the American Ceramic Society*, vol. 78, pp. 2374-2380.

Tomar, V.; Zhai, J.; Zhou, M. (2004): Bounds for element size in a variable stiffness cohesive finite element model. *International Journal for Numerical Methods in Engineering*, vol. 61, pp. 1894-1920.

Van Torne, L. (1966): Twinning in β-silicon carbide. *Physica Status Solidi B*, vol. 14, pp. 123-126.

Vanderwalker, D.; Croft, W. (1988): Dislocations in shock-loaded titanium diboride. *Journal of Materials Research*, vol. 3, pp. 761-763.

White, R.; Dickey, E. (2011): The effects of residual stress distributions on indentation-induced microcracking in B_4C-TiB_2 eutectic ceramic composites. *Journal of the American Ceramic Society*, vol. 94, pp. 4032-4039.

Zhao, Y.; Qian, J.; Daemen, L. ; Pantea, C.; Zhang, J. et al. (2004): Enhancement of fracture toughness in nanostructured diamond-SiC composites. *Applied Physics Letters*, vol. 84, pp. 1356-1358.